Effects of the Electron Polarization on Dynamic Nuclear Polarization in Solids

Journal:	*Physical Chemistry Chemical Physics*
Manuscript ID:	CP-ART-12-2014-005625.R1
Article Type:	Paper
Date Submitted by the Author:	19-Jan-2015
Complete List of Authors:	Hovav, Yonatan; Weizmann Institute of Science, Chemical Physics Shimon, Daphna; Weizmann Institute of Science, Chemical Physics Kaminker, Ilia; Weizmann Institute of Science, Chemical Physics Feintuch, Akiva; Weizmann Institute of Science, Chemical Physics Goldfarb, Daniella; Weizmann Institute of Science, Chemical Physics Department Vega, Shimon; Weizmann Institute of Science, Department of Chemical Physics

Effects of the Electron Polarization on Dynamic Nuclear Polarization in Solids

Hovav Y., Shimon D., Kaminker I., Feintuch A., Goldfarb D,. and Vega S.*

Weizmann institute of Science, Rehovot , Israel
*shimon.vega@weizmann.ac.il

Abstract

Dynamic Nuclear Polarization (DNP) experiments on solid dielectrics can be described in terms of the Solid Effect (SE) and Cross Effect (CE) mechanisms. These mechanisms are best understood by following the spin dynamics in electron-nuclear and electron-electron-nuclear model systems, respectively. Recently it was shown that the frequency swept DNP enhancement profiles can be reconstructed by combining basic SE and CE DNP spectra. However, this analysis did not take into account the role of the electron spectral diffusion (eSD), which can result in a dramatic loss of electron polarization along the EPR line.

In this paper we extend the analysis of DNP spectra by including the influence of the eSD process on the enhancements. We show for an electron-electron-nuclear model system that the change in nuclear polarization can be caused by direct MW irradiation on the CE electron transitions, resulting in a direct CE (dCE) enhancement, or by the influence of the eSD process on the spin system, resulting in nuclear enhancements *via* a process we term the indirect CE (iCE). We next derive the dependence of the basic SE, dCE, and iCE DNP spectra on the electron polarization distribution along the EPR line and on the MW irradiation frequency. The electron polarization can be obtained from ELDOR experiments, using a recent model which describes their temporal evolution in real samples. Finally, measured DNP and ELDOR spectra, performed on a 40 mM TEMPOL sample at 10-40 K, are analyzed. It is shown that the iCE is the major mechanism responsible for the bulk nuclear enhancement at all temperatures.

1 Introduction

During Dynamic Nuclear Polarization (DNP) the high electron Boltzmann polarization is transferred to neighboring nuclei *via* microwave (MW) irradiation, resulting in dramatic enhancements of NMR and MRI signals. Although known for more than 60 years[1, 2, 3], DNP has recently regained interest due to new technological and methodological developments. These has made it possible to enhance a large variety of samples, with the experiments performed using high field solid state magic angle spinning (MAS) NMR[4, 5, 6, 7, 8, 9, 10], or high resolution NMR and MRI using dissolution DNP[11]. This development has also led to a renewed interest in the theory of DNP.

The DNP mechanism in non-conducting solid samples can be explained by relying on the spin dynamics of microscopic spin systems which result in the Solid Effect[3] (SE) and Cross Effect[12, 13, 14, 15, 16] (CE) DNP mechanisms. The SE-DNP mechanism relies on MW irradiation at electron-nuclear zero quantum (ZQ) and double quantum (DQ) "forbidden" transition frequencies for its polarization transfer from the electrons to coupled nuclei. The CE mechanism relies on the presence of a nucleus coupled to a pair of interacting electrons with resonance frequencies separated by the nuclear Larmor frequency (the so called CE condition) resulting in an energy level degeneracy between electron-electron-nuclear spin states. Early on, it was understood that the NMR signals are enhanced by an electron-electron-nuclear cross relaxation mechanism, induced by spin-spin interactions and energy level degeneracies, in the presence of an electron polarization gradient[16, 17, 18] generated by a small hyperfine perturbation of the system[17]. Later, this description was extended to involve full state mixing at the CE condition[19, 20], in order to explain the CE mechanism in terms of a MW driven polarization transfer in static samples[21, 22] - in analogy to the SE mechanism but with higher MW irradiation efficiency. In addition, under MAS conditions the CE mechanism was recently explained in terms of fast passages through the CE conditions within each rotor period[23, 24], where electron polarization gradients are transferred to the nuclei.

The shapes of the DNP spectra, i.e. the NMR enhancements as a function of MW frequency, have been used to study and differenciate between the DNP mechanisms[15, 25, 26, 27, 28, 29, 30, 31, 32, 33, 34, 35].Recently, it was shown that the intensity and shape of cw DNP spectra can be analyzed in terms of linear combinations of basic SE DNP and CE DNP line-shapes[36, 37, 38] derived from a quantum mechanical (QM) based model calculations[39, 22]. In particular, recorded changes in the DNP line-shapes with temperature were attributed to changes in the relative contributions of these DNP mechanism. While doing this it was assumed that the DNP enhancement efficiency at each MW frequency depends linearly on the fraction of electrons taking part in the enhancement mechanisms. However, while electron depolarization due to direct MW irradiation was considered in these models, the redistribution of polarization due to the electron spectral diffusion (eSD) mechanism[40, 41, 42, 43, 44] was not taken into account. Very recently, Siaw *et al.* [45] explained changes in DNP enhancement efficiencies using changes in the electron depolarization generated by direct MW irradiation and by the eSD mechanism. However this did not involve actual measurements of the electron polarization distribution.

Direct measurements of the electron depolarization on DNP samples by electron-electron double resonance (ELDOR) spectroscopy[46] showed that the eSD process causes large electron depolarizations [47, 48]. Very recently a theoretical model was introduced that enables simulations of the experimental electron polarization distributions by solving a set of coupled rate equations for the polarizations composing the EPR line[48]. This model includes the effects of the MW irradiation and spin-lattice relaxation, as well as the effect of the eSD mechanism, on the electron polarizations.

In this work we reexamine the DNP mechanisms leading to the DNP spectra, while taking the eSD induced electron depolarization into account. We again base our descriptions on the QM derived spin dynamics of model systems[22] and reformulate how the spin state degeneracies of a “CE electron pair” at a CE condition result in CE DNP enhancements. In particular, it is shown analytically and based on simulations that these enhancements are a result of a MW irradiation that directly saturates one of the transitions of the CE electron pair (dCE DNP) or that saturates the transitions of other electrons which then indirectly depolarize the CE electron pair (iCE DNP) *via* eSD. Next, analytic expressions are derived to correlate the electron polarization distribution in a real sample with the line-shapes of the basic SE , dCE, and iCE DNP spectra. Finally, examples of experimental DNP line-shapes, obtained from a sample of 40 mM TEMPOL at 10, 20 and 40 K, are shown. They are analyzed by calculating the line-shapes of the different mechanisms, taking into account electron polarization distributions obtained by fitting simulated ELDOR spectra with measured ones. Here we show that in this sample the enhancement originates mainly from the iCE-DNP mechanism and the changes in the DNP spectra as a function of temperature can be attributed to the change in the electron polarization profiles.

2 Experiments and Simulations

2.1 Experiments

All EPR and NMR signals were collected in a 3.34 T magnet using our combined EPR (operating around 95 GHz) and NMR (at 144 MHz for protons) spectrometer described in Ref. [49]. Combined ELDOR and DNP experiments (ELDOR/DNP) and spin-lattice relaxation measurements were conducted on a sample that was prepared by dissolving 40 mM TEMPOL radical in a 50:50 v% mixture of dimethyl sulfoxide (DMSO) and H_2O. 25 μl of this solution was placed in a Teflon sample holder that was inserted into the NMR coil located between the MW horn and reflection plate of the hybrid EPR/NMR spectrometer. TEMPOL and DMSO were purchased from Sigma-Aldrich. MW excitation and detection were performed using a home-built bridge with two MW channels, controlled by the Specman4EPR software package[50]. RF excitation and detection were controlled by an APOLLO spectrometer from Tecmag inc. The APOLLO is externally triggered by a logic pulse generated by the EPR spectrometer. The probe-head and sample are located inside a Janis Research inc. liquid helium flow cryostat, and in the present study experiments were performed at 10, 20, and 40 K.

The pulse sequence used during the ELDOR/DNP experiments is shown schematically in Fig. 1. It starts with an RF pulse train on the ^{1}H nuclei, resulting in their saturation. Next, a cw-MW excitation pulse at a variable frequency ω_{excite} and a magnitude of $\omega_1/2\pi \simeq$ 600 kHz was applied for a duration of t_{excite}, using one of the two EPR channels. This was followed by the acquisition of EPR and NMR signals using a $\{\frac{\pi}{2} - \tau - \frac{\pi}{2}\}$ echo pulse sequences. For the EPR acquisition 450 ns MW pulses were applied and echo signals were detected at a frequency ω_{detect}, using the second MW channel. The intensity of the EPR and NMR signals were determined by integration over the echo signals. Thermal equilibrium NMR signals were acquired in the same manner but without MW irradiation and the DNP enhancements were calculated by the ratio between the signals acquired with and without MW irradiation.

The electron and nuclear relaxation times, T_{1e} and T_{1n}, were determined by analyzing the recovery of the echo signals after signal saturation by a long cw MW pulse (using $t_{excite} > T_{1e}$) and a RF pulse train, respectively.

2.2 Simulations

Three computer programs were used in this work: one for evaluating the spin dynamics of small spin systems, composed of spin-$\frac{1}{2}$ electrons and ^1H nuclei, by following the temporal

Figure 1: A schematic representation of the ELDOR/DNP sequence used during the experiments. This includes a pulse train saturating the ^{1}H nuclei, followed by an MW irradiation at a frequency ω_{excite} for a duration t_{excite}, and the detection of an EPR echo at a frequency ω_{detect} and an NMR echo at ω_{1H} generated by an RF pulse. This was followed by a delay of about $5T_{1n}$.

behavior of the electron and nuclear polarizations. This was done by solving the Liouville - von Neumann equation for the spin density operator in Liouville space, or in a reduced population space[39, 51, 22]. The second program was used for calculating the electron polarization distribution along the EPR line during ELDOR/DNP, by solving a set of coupled rate equations for the polarization of electrons in frequency bins composing the inhomogeneously broadened EPR spectrum and of the nuclear polarization[48]. The third program was used for simulating the basic DNP line-shapes of the different DNP mechanisms, while taking into account the contribution of the different electron packets composing the EPR line and their polarization. The theoretical bases of the first two programs will be only briefly discussed here, as they were already introduced earlier, and of the latter will be presented in section 4.

2.2.1 Full and reduced Liouville space calculations for small model spin systems

To calculate the spin evolution of a model spin system during MW irradiation we must first construct its spin Hamiltonian and the spin relaxation superoperator. The MW rotating frame Hamiltonian of the systems considered here, containing interacting electrons ($S_\imath = 1/2$) and ^1H nuclei ($I_\ell = 1/2$), has the same general form as in Ref. [22]:

$$H = \sum_{\imath<\imath',\ell} \{\Delta\omega_{e,\imath} S_{z,\imath} - \omega_n I_{z,\ell} + A_{z,\imath\ell} S_{z,\imath} I_{z,\ell} + A^+_{\imath,\ell} S_{z,\imath} I^+_\ell + A^-_{\imath\ell} S_{z\imath} I^-_\ell + D_{\imath\imath'}(3S_{z,\imath}S_{z,\imath'} - \overline{S}_\imath.\overline{S}_{\imath'}) + \omega_1 S_{x,\imath}\}. \tag{1}$$

This Hamiltonian includes the electron Zeeman interaction terms, $\Delta\omega_{e,\imath} =\omega_{e,\imath} - \omega_{excite}$, where $\omega_{e,\imath}$ is the frequency of electron $\imath$ and ω_{excite} is the MW excitation frequency; the nuclear Larmor frequency ω_n of all nuclei; the secular and pseudo-secular hyperfine interaction coefficients $A_{z,\imath\ell}$ and $A^\pm_{\imath\ell}$ of the electron-nuclear spin pairs $\imath - \ell$; and the dipolar coupling constants $D_{\imath\imath'}$ between the electrons $\imath$ and $\imath'$. In addition, a MW irradiation Hamiltonian is added to H, given by $H_{MW} = \omega_1 \sum_\imath S_{x,\imath}$, where ω_1 is the irradiation intensity.

Each spin system is defined by a vector $\overline{\rho}(t)$, composed of all spin density matrix elements, in Liouville space, satisfying:

$$\frac{d}{dt}\overline{\rho}(t) = (i\widehat{H} + \widehat{\Gamma})\overline{\rho}(t), \tag{2}$$

where $\widehat{H}$ is the Liouvillian derived from H, and $\widehat{\Gamma}$ is the relaxation superoperator. In general, this equation is presented in the Liouville space defined by the eigenstates $|\lambda_k\rangle$ of the spin system $H_0 = H - \omega_1 \sum_\imath S_{x,\imath}$. In this representation it is easy to separate the longitudinal relaxation, which affects only the populations of the system, and the transverse relaxation, affecting only the coherences.

The relevant relaxation rates influencing the ρ_{kk} and $\rho_{k'k'}$ populations of the eigenstates $|\lambda_k\rangle$ and $|\lambda_{k'}\rangle$ are defined by their matrix elements in $\widehat{\Gamma}$. Here we consider the basic electron and nuclear spin-lattice relaxation rates, with a timescale of T_{1e} and T_{1n} respectively, and in addition an electron-electron dipolar driven cross-relaxation rate, with a timescale of $T_{1D,\imath\imath'}$[52]. The latter is used as a model for the eSD process. These relaxation mechanisms restore the system to its thermal equilibrium state, given by the Boltzmann ratios $\rho_{kk}/\rho_{k'k'} = \exp(-\omega_{kk'}\hbar/k_BT)$, were $\hbar$ and k_B are the Planck and Boltzmann constants, and $\omega_{kk'}$ is the difference between the energies of the $|\lambda_k\rangle$ and $|\lambda_{k'}\rangle$ eigenstates. For simplicity a single spin-spin relaxation time, T_{2e}, was considered to take care of the decay of all relevant electron coherences $\rho_{kk'}$.

Calculations were also performed in a reduced Liouville space spanned by the populations $p_k = \rho_{kk}$. The interaction Liouvillian in the diagonal representation does not influence these populations, and MW irradiation is represented by off diagonal matrix elements $w_{kk'}$ added to a superoperator $\widehat{W}$ composed of the spin lattice rate matrix elements of $\widehat{\Gamma}$ discussed above. The MW rate elements $w_{kk'}$ are a function of the matrix elements$\langle\lambda_k|H_{MW}|\lambda_{k'}\rangle$, the spin-spin relaxation rate T_{2e}, and the off resonance values $(\omega_{kk'} - \omega_{excite})$[39, 51]. The population vector $\overline{p}(t)$, composed of all p_k populations, satisfies the equation

$$\frac{d}{dt}\overline{p}(t) = \widehat{W}\overline{p}(t). \tag{3}$$

This population description of the spin systems results in the same spin evolution as the full Liouville space calculation as long as the coherent evolution of the system can be neglected. For example, this is the case when one of the electrons is initially saturated without residual coherences, and the evolution of the system is solely governed by spin-lattice relaxation rates (including T_{1D}^{-1}).

The polarizations of the nuclei and electrons can be calculated by solving eqs. 2 or 3, and transferring their solutions $\overline{\rho}(t)$ and $\overline{p}(t)$ to the Hilbert space spin density operator $\rho(t)$ and evaluating

$$\begin{array}{rcl} P_{e,\imath}(t) & = & -z\mathrm{Tr}(S_{z,\imath}\rho(t)) \\ P_{n,\ell}(t) & = & z\mathrm{Tr}(I_{z,\ell}\rho(t)) \end{array}, \tag{4}$$

where z normalizes the $T \rightarrow 0$ polarizations to one.

In section 3.2 numerical simulations of the steady state electron and nuclear polarizations of model systems experiencing MW irradiation will be presented.

2.2.2 Calculation of the electron polarization distribution in macroscopic systems

The electron polarization distribution along the EPR line can be evaluated using a model that was recently introduced by Hovav et al. [48] for simulating ELDOR spectra. This theoretical model calculates the dynamics of the polarizations of the electrons in N frequency bins that compose the inhomogeneously broadened EPR line of the radicals. These frequency bins have average frequencies given by $\omega_j = \omega_{j=1} + (j-1)\Delta_{bin}$, where Δ_{bin} is the frequency width of the bins and $j = 1, ..., N$. Each of the bins is associated with a fraction f_j of the total number of electrons in the system ($\sum_j f_j = 1$), as given by the EPR line, and has an average electron polarization $P_{e,j}(t)$. The temporal evolution of these electron polarizations can then be calculated by solving rate equations for $P_{e,j}(t)$ and (for simplicity) a single bulk nuclear polarization $P_n(t)$. These calculations take into account: the effects of the MW irradiation of strength ω_1 applied at a frequency $\omega_{excite,j'} = \omega_{j=1} + n_{j'}\Delta_{bin}$, where $n_{j'}$ is an integer; the spin-spin relaxation time T_{2e} (which is expected to be longer than the phase memory time of the system); the electron and nuclear spin-lattice relaxation rates T_{1e}^{-1} and T_{1n}^{-1}; and the eSD mechanism that causes polarization exchange between all $P_{e,j'}(t)$ and $P_{e,j}(t)$ with exchange rates defined by $w^{eSD} = \frac{\Lambda^{eSD}}{(\omega_j - \omega_{j'})^2}$, where Λ^{eSD} is a phenomenological coefficient. In this model the SE induced electron-to-nuclear polarization transfer is present in the form of a MW irradiation field on the ZQ and DQ transitions that has an effective strength $\omega_1^{SE} = (\overline{A}^{\pm}/2\omega_n)\omega_1$, where $\overline{A}^{\pm}$ is a coefficient representing the average hyperfine interaction between an electron and the nuclei. The parameters T_{2e}, Λ^{eSD} and $\overline{A}^{\pm}$ are determined by fitting simulated ELDOR profiles to experimental ones. Following this procedure the electron polarization distribution $P_e(\omega_{detect})$ for a given ω_{excite} frequency and t_{excite} irradiation time can be calculated.

3 The Cross Effect mechanism in model spin systems

In the following we will consider the CE mechanism in model spin systems, and show how polarization is transferred from the electrons to the nuclei as a result of the CE degeneracy. This transfer can occur when the electron transitions are directly (partially or fully) saturated by MW irradiation[21, 22], which we term dCE, or when these transitions are not excited by the MW field but are (partially) saturated indirectly *via* the eSD mechanism, which we will term iCE. In practice, in section 4 we will extend this iCE process to real systems by integrating over the iCE DNP contributions from all electron pairs at a CE condition in this system.

At first we will derive an equation expressing the relationship between the steady state nuclear and electron polarizations in model systems at the CE condition. The accuracy of this expression and its limitations will then be checked using numerical simulations. These will then be extended to further investigate the iCE mechanism, in analogy to earlier studies of the dCE mechanism in Ref. [22].

3.1 The correlation of the electron and nuclear polarizations

In this section we reexamine the value of the static DNP enhancement induced by MW irradiation on a pair of electrons at one of its CE conditions. This is done for a simple three-spin system composed of a pair of dipolar coupled electrons, e_a and e_b, with resonance frequencies $\omega_a \leq \omega_b$, and a nucleus n that is hyperfine coupled to the electrons. This spin system can be characterized by eight populations $p(\chi_a, \chi_b, \chi_n)$ corresponding to the eight eigenstates $|\chi_a, \chi_b, \chi_n\rangle$ with $\chi = \alpha, \beta$, and where, for simplicity, we do not change these product state assignments despite possible state mixing due to the dipolar and hyperfine interactions.

To derive an expression that correlates the steady state nuclear polarization to the electron polarizations we consider an ideal case in which the SQ transitions of each electron are equally affected by the MW irradiation and the relaxation mechanism. This is not an obvious assumption, since the electron SQ transitions are split by the electron dipolar interaction, D_{ab}, and the secular hyperfine interactions, $A_{z,a}$ and $A_{z,b}$. Thus, in the dCE case this assumption holds when the MW equally excites the two transitions of one of the electrons, which will be the case when $\omega_1\sqrt{T_{1e}/T_{2e}} \gg |D_{ab}| + |\frac{1}{2}A_z|$ (assuming $\omega_1^2 T_{1e}T_{2e} \gg 1$). In the iCE case we can expect the dipolar cross relaxation rates to have the same effect on both of these transitions, because the spectral densities of the fluctuating dipolar interactions, which are the source of the dipolar cross relaxation, should be the same for both transitions. When these assumptions hold we can express the ratios between the populations of our system in a simple manner using:

$$\frac{p(\alpha_a, \chi_b, \chi_n)}{p(\beta_a, \chi_b, \chi_n)} = \eta_a; \quad \frac{p(\chi_a, \alpha_b, \chi_n)}{p(\chi_a, \beta_b, \chi_n)} = \eta_b; \quad \frac{p(\chi_a, \chi_b, \beta_n)}{p(\chi_a, \chi_b, \alpha_n)} = \eta_n, \tag{5}$$

where the three η parameters can have different values. At thermal equilibrium these $\eta-$ratios are equal to the Boltzmann ratios $\epsilon_{a/b/n} = \exp(-\omega_{a/b/n}\hbar/k_BT)$, and we can expect that in general $\epsilon_{a/b} \leq \eta_{a/b} \leq 1$, where $\eta_{a/b} = 1$ corresponds to full saturation of electron

a or b. Far removed from the CE condition and when the MW irradiation does not affect the ZQ and DQ transitions, the nucleus will remain at its thermal value, $\eta_n = \epsilon_n$.

Using these η values, the populations can be expressed as:

$$\begin{array}{rcccrcc} p(\beta_a,\beta_b,\beta_n) & = & c\eta_n & ; & p(\beta_a,\beta_b,\alpha_n) & = & c \\ p(\beta_a,\alpha_a,\beta_n) & = & c\eta_b\eta_n & ; & p(\beta_a,\alpha_b,\alpha_n) & = & c\eta_b \\ p(\alpha_a,\beta_b,\beta_n,) & = & c\eta_a\eta_n & ; & p(\alpha_a,\beta_b,\alpha_n) & = & c\eta_a \\ p(\alpha_a,\alpha_b,\beta_n) & = & c\eta_a\eta_b\eta_n & ; & p(\alpha_a,\alpha_b,\alpha_n) & = & c\eta_a\eta_b \end{array}, \tag{6}$$

where c is a normalization constant such that $\sum_\chi p(\chi_a,\chi_b,\chi_n) = 1$. The electron and nuclear polarizations are then given (neglecting possible state mixing) by

$$\begin{array}{rcll} P_a & = & \sum_{\chi_b,\chi_n} p(\beta_a,\chi_b,\chi_n) - p(\alpha_a,\chi_b,\chi_n) & = (1-\eta_a)/(1+\eta_a) \\ P_b & = & \sum_{\chi_a,\chi_n} p(\chi_a,\beta_b,\chi_n) - p(\chi_a,\alpha_b,\chi_n) & = (1-\eta_b)/(1+\eta_b) \\ P_n & = & \sum_{\chi_a,\chi_b} p(\chi_a,\chi_b,\alpha_n) - p(\chi_a,\chi_b,\beta_n) & = (1-\eta_n)/(1+\eta_n) \end{array}. \tag{7}$$

When the system is at the CE condition, $\omega_b - \omega_a \simeq \omega_n$, the energies corresponding to the $|\alpha_a,\beta_b,\beta_n\rangle$ and $|\beta_a,\alpha_b,\alpha_n\rangle$ states are equal, and these states become strongly mixed[19, 20, 21, 22]. The MW irradiation and relaxation processes, which are the source of the deviations of the $\eta_{a/b}$ from $\epsilon_{a/b}$, must then have the same effect on the populations of these mixed states, such that:

$$p(\alpha_a,\beta_b,\beta_n) = p(\beta_a,\alpha_b,\alpha_n). \tag{8}$$

This condition sets a constraint on the populations of the overlapping DQ or ZQ and SQ electron transitions and has therefore a strong effect on all populations in the system. Inserting this equality into the expressions in eq. 6 results in a dependence between the $\eta-$ratios given by

$$\eta_n = \eta_b/\eta_a, \tag{9}$$

and using this together with eq. 7 gives the the dependence of P_n on P_a and P_b:

$$P_n = \frac{P_b - P_a}{1 - P_b \times P_a}. \tag{10}$$

Once again, here the polarizations are defined as $P_{a/b/n} \rightarrow 1$ for $T \rightarrow 0$. Under the initial assumptions this relationship holds for any pair of P_a and P_b values, including their thermal equilibrium values: insertion of $P_a = \tanh(-\omega_a\hbar/2k_BT)$ and $P_b = \tanh(-(\omega_a+\omega_n)\hbar/2k_BT)$ into the right side of eq. 10 results in $P_n = \tanh(-(\omega_a+\omega_n)\hbar/2k_BT + \omega_a\hbar/2k_BT) = \tanh(-\omega_n\hbar/2k_BT)$ for all temperatures. At the high temperature limit, where $P_b \times P_a \ll 1$, the polarization relation reduces to

$$P_n \simeq (P_b - P_a). \tag{11}$$

Eq. 10 has the same form as presented by Hwang and Hill [16], and eq. 11 is same as derived by Atsarkin et al.[18] and Wollan[17]. The latter two are based on a cross relaxation rate derived from a perturbation theory approach. The use of perturbation theory for the derivation of the CE rates [18, 17, 19, 53] is however problematic in the presence of large state mixing, as in the CE case.

In the following the validity of eq 10 and the limits of eq. 5 will be tested using numerical simulations for both the iCE and dCE mechanisms. The relationship between the polarizations given in eq. 10 will be used in section 4, when considering the DNP line-shapes in macroscopic systems.

3.2 Numerical simulations

In order to demonstrate the validity of eq. 10 we calculated the steady state DNP polarizations of a model four-spin system under MW irradiation. This system is composed of a pair of electrons, e_a and e_b, and a nucleus n, with Larmor frequencies satisfying $\omega_b - \omega_a \approx \omega_n$, and an additional electron e_c. The electrons e_a and e_b are dipolar coupled and n is hyperfine coupled to e_b. Electron e_c is introduced in order to allow for a reduction of the polarization of electrons e_a and e_b without direct MW irradiation, namely by the $T_{1D,ac}^{-1}$ and $T_{1D,bc}^{-1}$ rates. These rates originate from fluctuations of the dipolar interaction between these electrons. Since the static part of this interaction complicates the system, as shown in the SI, it is assumed to be small enough that it can be ignored in the static Hamiltonian, while it is still a source for the dipolar cross-relaxation. The steady state $P_a(t)$, $P_b(t)$, and $P_n(t)$ values of this system were simulated for both the iCE mechanism and dCE mechanism, and the resulting polarizations were inserted in eq. 10 in order to verify whether they obey this relationship. The parameters used in the simulations are summarized in Table 1 and in the figure caption of Figs. 2 and 3. In particular, T =5 K was chosen, resulting in thermal electron polarization about equal to 0.42.

In the iCE case the MW irradiation was applied on resonance for electron e_c ($\omega_{excite} = \omega_c$) and far off resonance from e_a and e_b. The polarizations of the latter are then reduced due to the action of the $T_{1D,ca}^{-1}$ and $T_{1D,cb}^{-1}$ cross relaxation rates. The simulations were conducted based on eq. 3, and the polarizations were calculated for a variety of cross relaxation rates. The calculated *vs.* simulated $P_n(t)$ values are plotted in Fig. 2 for systems with $D_{ab}/2\pi = 0.8$ MHz (broad black line) and $D_{ab}/2\pi = 20$ MHz (narrow green line). The calculated $[P_a(t), P_b(t)]$ pairs obtained are plotted in the insert of the figure. The validity of the assumption expressed by eq. 5 was also tested, by comparing the simulated populations, p_k^{sim}, with calculated ones, p_k^{calc}. The calculated populations were obtained by the deriving values of the η parameters from the simulated $P_{a/b/n}$ values using eq. 7, and inserting these values into eq. 6. The maximal difference between the simulated and calculated populations, $|(p_k^{sim} - p_k^{calc})/p_k^{sim}|$ was about 0.5%.

For the dCE case the polarizations were calculated for different ω_{excite} MW frequencies close to the SQ transitions of the electrons e_a and e_b, and all T_{1D}^{-1} cross relaxation rates were set to zero. These simulations were performed solving eq. 2. The simulated (solid black lines) and calculated (dotted red lines) steady state P_n values are shown in Fig. 3 for $D_{ab}/2\pi = 0.8$ MHz, with the calculated values obtained using eq. 10. As can be seen there is a very good agreement between the two. In this system both dipolar satellite transitions are about equally affected by the MW irradiation for any ω_{excite} frequency. This can be seen from the electron polarization, drawn in gray. The validity of the assumption expressed in eq. 5 was tested as before, resulting in a maximal error of about 1.5% (see SI). Performing the simulation with a higher ω_1 value (6 MHz), where the MW irradiation can affect the polarization of both electrons simultaneously (data not shown) resulted again in a very good agreement between the calculated and predicted P_n and p_k values.

In order to show a case where the SQ transitions of the electrons are not equally affected by the MW irradiation, we now consider a system with a large dipolar interaction, $D_{ab}/2\pi =$ 20 MHz. The resulting simulated and calculated steady state P_n values are plotted in Fig. 3b, showing an unexpected similarity between the two, despite the large difference (as high as 20%) between the p_k^{sim} and p_k^{calc} populations, as shown in the SI. Thus it seems that due to the relaxation in the system eq. 10 is a good approximation even when the assumptions given in eq. 5 are partially violated.

Figure 2: Calculated P_n^{calc} vs. simulated P_n^{sim} nuclear polarization values under the iCE DNP. The simulation was performed on a model spin system at the CE condition using the parameters given in table 1, with $\omega_{excite} = \omega_c$ and for $T_{1D,ac}^{-1}$ and $T_{1D,b,c}^{-1}$ relaxation rates in the range of about $0.02T_{1e}$ to $50T_{1e}$. A $D_{ab}/2\pi$ interaction of 0.8 (broad black line) or 20 (narrow green line) MHz was used. P_n^{calc} was calculated from eq. 10 for each choice of $T_{1D,ac}^{-1}$ and $T_{1D,b,c}^{-1}$, using the simulated P_a and P_b electrons polarizations, as plotted in the insert using the same color code (in the range of 0 to 0.43).

An important aspect of the CE mechanism is the dependence of the nuclear enhancement on the deviation from the CE condition. This was already investigated in Ref. [22] for the dCE mechanism, and is here extended to the iCE case. This is done for the spin system described above by varying the difference between the frequencies of electrons e_a and e_b in

Figure 3: A comparison between the calculated (red dashed lines) and simulated (black lines) steady state nuclear polarizations $P_n(t)$ as a function of ω_{excite}, during a dCE DNP experiment on a {e-e-n} three-spin model system. This system at its CE condition has parameters given in table 1, with the T_{1D} rates set to zero. The electron dipolar interaction constant $D_{ab}/2\pi$ was set equal to (a) 0.8 or to (b) 20 MHz. Eq. 10 was used to derive $P_n(t)$ from the simulated steady state electron polarizations $P_{e,a/b}(t)$. For clarity these electron polarizations are added to the figure as gray lines.

the vicinity of $\omega_b - \omega_a = \omega_n$. Simulated steady state $P_n(t)$ values are plotted in Fig. 4 (solid black line) as a function of $(\omega_b - \omega_a - \omega_n)$, using the parameters given in Table 1. As expected, a clear maximum, satisfying eq. 10 (gray line), appears at the CE condition. The width of the $P_n(t)$ profile around the CE condition depends on the effective interaction strength between the degenerate states, with a magnitude of the order of $A^{\pm}_{bn} D_{ab}/2\omega_n$[19, 20, 22]. In addition, the value of T_{1n} opposing the polarization enhancement also influences the width of the profile. To show an example of this dependence we calculated three additional $P_n(t)$ profiles by reducing the original value of $A^{\pm}_b$ by a factor of two, as plotted in the figure (black dashed line). Reduction of D_{ab} by the same factor or the value of T_{1n} by a factor of four resulted in almost identical curves (not shown). Thus in all cases the maximal enhancement is reached at the CE condition, but the decay of the iCE enhancement as a function of $(\omega_b - \omega_a - \omega_n)$ becomes faster for smaller $A^{\pm}_b$ or D_{ab} or shorter T_{1n} values, as in the dCE mechanism[22].

Figure 4: Steady state nuclear polarization as a function of the CE matching condition in the iCE case. Simulations were performed using $A^{\pm}_2/2\pi$ values equal to 1 MHz (solid black lines) or 0.5 MHz (dashed line) for different ω_b values around the $\omega_b - \omega_a - \omega_n = 0$ CE condition. The MW field was applied at ω_c. The rest of the parameters are given in Table 1. The gray line indicates the expected CE enhancement in the ideal case based on the electron polarizations given by eq. 10.

The iCE mechanism can also be studied by following the temporal evolution of the spin polarizations. In Fig. 5 the time evolution of the electron polarizations are plotted for the CE condition, $\omega_b - \omega_a \simeq \omega_n$ (solid lines) and for an offset of 50 kHz from this condition (dashed lines). All simulation parameters are given in Table 1, and the MW frequency was set at ω_c. $P_c(t)$ approaches zero in a relatively short time, and is not shown. The $P_b(t)$ (red) and $P_a(t)$ (purple) polarizations reach their steady state values in a timescale of T_{1e} (left vertical dotted black line). At the CE condition, $P_n(t)$ (blue) reaches the value predicted by eq. 10 (gray line) within the same timescale. This differs from the dCE mechanism, where the change in the electron and nuclear polarizations has a fast component, originating from the MW irradiation on the electron and electron-nucleus transitions, and a slower component originating from

T_{1e}[22]. When the CE condition is not met the iCE nuclear hyperpolarization buildup time becomes longer, and can become as long at T_{1n} (right vertical dotted black line). When this happens the maximal $P_n(t)$ value is reduced due to the action of T_{1n}.

Figure 5: Temporal evolution of the nuclear (blue) and electron polarizations (red and purple) during iCE-DNP. Simulations were performed on a system at the CE condition (solid lines) or 50 kHz removed from it (dashed lines), using MW at $\omega_{excite} = \omega_c$. All other simulation parameters are given in Table 1. The gray line indicates the expected steady state CE nuclear polarization in the ideal case derived from the electron polarizations using eq. 10. The horizontal dashed black lines indicate the T_{1e} and T_{1n} values used in the simulations.

Finally, as shown previously for the dCE mechanism, the dipolar and hyperfine interactions split the CE conditions and reduces the maximum nuclear polarizations [22, 54]. The same trends can be seen in the case of the iCE mechanism, as shown in the SI.

Parameter	Value
T	5 K
$A_b^{\pm}/2\pi$	1 MHz
$D_{ab}/2\pi$	0.8 MHz
$\omega_1/2\pi$	0.6 MHz
T_{1e}	10 ms
T_{1n}	1 s
T_2	10 μs
$T_{1D,ab}/T_{1D,ac}/T_{1D,bc}$	1/1/0 ms
$(\omega_{e,b} - \omega_{e,a})/2\pi$	~144 MHz
$(\omega_{e,c} - \omega_{e,a})/2\pi$	-160 MHz

Table 1: Parameters used during the iCE and dCE simulations. The difference between the electron frequencies, $\omega_{e,b} - \omega_{e,a}$ at the CE condition was evaluated up to 1 Hz based on the mixing of states in the spin system. Changes in these values are given in the figure captions.

4 Calculation of the DNP-spectra for the different DNP mechanisms in macroscopic systems

In this section we derive expressions for the steady state DNP line-shapes corresponding to the SE, dCE and iCE mechanisms in macroscopic systems with inhomogenously broadened EPR lines. These expressions are derived taking into account the electron polarization distributions and the relation between the nuclear and electron polarizations derived in Section 3. In order to calculate the DNP enhancement $S_n(\omega_{excite})$ as a function of the

MW frequency ω_{excite}, we make the following assumptions: (i) The DNP enhancement scales linearly with the fraction of electrons that transfer their polarization to the nuclei[36, 37, 38]. (ii) This fraction can be derived from the normalized EPR line, $f(\omega_e)$. Thus the electrons are treated as having single SQ transitions while possible splittings due to the dipolar or hyperfine interactions are not considered. (iii) At the CE condition, the dependence of the nuclear polarization on the electron polarizations is given by eq. 10. (iv) The enhancements derived for the different DNP mechanisms can be calculated independently[36, 37, 38]. And finally, (v) the electron polarization profiles $P_e(\omega_e;\omega_{excite})$ are known. This last assumption implies that $P_e(\omega_e;\omega_{excite})$ can be derived independently of the nuclear DNP enhancement *via* a fitting procedure applied to experimental ELDOR date[48]. We will not try to simulate the actual intensities of the frequency dependent DNP enhancement spectra, $E_n(\omega_{excite})$, but rather their line-shapes. One of the reasons for this is that at this stage we do not take into account effects influencing these intensities, such as those originating from T_{1n} relaxation and nuclear spin diffusion.

Using the above assumptions we can derive the shapes of the normalized basic DNP spectra, $S_M(\omega_{excite})$, with $M = SE$, dCE, iCE, and express the DNP enhancement of a sample in the from

$$E_n(\omega_{excite}) = k_{SE}S_{SE}(\omega_{excite}) + k_{dCE}S_{dCE}(\omega_{excite}) + k_{iCE}(S_{iCE}(\omega_{excite}) - S_{iCE,0}) + 1, \quad (12)$$

where k_M are constants that determine the relative contributions of the individual $S_M(\omega_{excite})$ spectra and the one is added to account for the thermal equilibrium value. The reason for the subtraction of the thermal equilibrium value $S_{iCE,0}$ of $S_{iCE}(\omega_{excite})$ from the iCE contribution will be discussed later on.

The basic SE DNP enhancement spectrum for MW irradiation at ω_{excite} is proportional to the $P_e(\omega^{\pm}_{excite};\omega_{excite})$ electron polarizations at frequencies $\omega^{\pm}_{excite} = \omega_{excite} \pm \omega_n + \delta\omega$, and to the relative number of these electrons $f(\omega^{\pm}_{excite})$. In order to include off resonance effects in the SE mechanism a function $g_{SE}(\delta\omega)$ (for example, with a Lorenzian line-shape) is introduced with a maximum at $g_{SE}(0)$. This maximum value depends on the MW power, and when $\omega_1 = 0$ the $g_{SE}(\delta\omega)$ value becomes zero. A normalization factor N_{SE} is introduced that sets the average of the magnitudes of the maximum and minimum enhancement of $S_{SE}(\omega_{exceite})$ equal one. As a result the maximal value of $g_{SE}(\delta\omega)$ does not have to be chosen. Thus for any ω_{excite} value we can write:

$$S_{SE}(\omega_{excite}) = N^{-1}_{SE}\int d(\delta\omega)\, g_{SE}(\delta\omega)\, \{s^{-}_{SE}(\omega_{excite}) - s^{+}_{SE}(\omega_{excite})\}, \quad (13)$$

where

$$s^{\pm}_{SE}(\omega_{excite}) = f(\omega^{\pm}_{excite})P_e(\omega^{\pm}_{excite};\omega_{excite}). \tag{14}$$

This can result in DNP enhancement outside of the EPR line as long as $f(\omega^{\pm}_{SE})$ and $g_{SE}(\delta\omega)$ have non-negligible values.

To express the basic CE DNP spectra in terms of a given electron $P_e(\omega_e;\omega_{excite})$ distribution, we use the expression correlating the nuclear polarization to the electron polarizations given in eq. 10. The CE enhancements are proportional to the relative number of contributing electron pairs at a CE condition, which is of the general form $f(\omega_e \pm \omega_n)f(\omega_e + \delta\Omega)$, where $\delta\Omega$ is the deviation from the CE condition. Introducing a two-dimensional (bell shaped) weight-function $g_{dCE}(\delta\omega,\delta\Omega)$ that expresses the enhancement reduction due to off resonance irradiation and the CE matching, and defining $\omega^0_{excite} = \omega_{excite} + \delta\omega + \delta\Omega$ we can write:

$$S_{dCE}(\omega_{excite}) = N^{-1}_{dCE}\iint d(\delta\omega)d(\delta\Omega)\, g_{dCE}(\delta\omega,\delta\Omega)\{s^{+}_{dCE}(\omega_{excite}) + s^{-}_{dCE}(\omega_{excite})\}, \tag{15}$$

where

$$s^{\pm}_{dCE}(\omega_{excite}) = f(\omega^{\pm}_{excite})f(\omega^{0}_{excite})\frac{P_e(\omega^{\pm}_{excite};\omega_{excite}) - P_e(\omega^{0}_{excite};\omega_{excite})}{1 - P_e(\omega^{\pm}_{excite};\omega_{excite}) \times P_e(\omega^{0}_{excite};\omega_{excite})}, \tag{16}$$

and N_{dCE} is a normalization factor. The widths of $g_{dCE}(\delta\omega,\delta\Omega)$ is of the order of $(\omega_1\sqrt{T_{1e}/T_{2e}}, A^{+}D_{ab}/\omega_n)$, and it is equal to zero for $\omega_1 = 0$. Except for the off resonance irradiation effects, there will be no enhancement outside the frequency range of the EPR line, where $f(\omega^{0}_{excite}) = 0$.

The expression for the iCE DNP spectrum depends on the polarization difference between all electron pairs at a CE condition. Taking into account the effect of the $\delta\Omega$ deviation from this condition on the iCE efficiency using the weight function $g_{iCE}(\delta\Omega)$, we can write:

$$S_{iCE}(\omega_{excite}) = N^{-1}_{iCE}\iint d\omega d(\delta\Omega) g_{iCE}(\delta\Omega) s_{iCE}(\omega;\omega_{excite}), \tag{17}$$

with

$$s_{iCE}(\omega;\omega_{excite}) = \{f(\omega+\omega_n)f(\omega+\delta\Omega)\frac{P_e(\omega+\omega_n;\omega_{excite}) - P_e(\omega+\delta\Omega;\omega_{excite})}{1 - P_e(\omega+\omega_n;\omega_{excite}) \times P_e(\omega+\delta\Omega;\omega_{excite})}. \tag{18}$$

As before, N_{iCE} is a normalization factor. Here DNP enhancement can be expected when we irradiate outside of the EPR line and electron polarization is lost *via* the SE process[48]. In practice, the above expression includes polarization losses also due to direct MW irradiation on the electrons. Doing this we sum over the contribution of all CE electron pairs, whether or not they are depolarized by direct or indirect MW irradiation. As such, effects originating from the direct MW irradiation are taken into account both in the dCE-DNP as well as the iCE-DNP line-shape. We must still make a distinction between dCE and iCE because their enhancement dynamics are not equal, as described around Fig. 5. Any additional contribution of the dCE mechanism is then given by the S_{iCE} line-shape.

Both $S_{SE}(\omega_{excite})$ and $S_{dCE}(\omega_{excite})$ are zero when the system is at its thermal equilibrium state, as achieved for example for far off resonance irradiation. However, the iCE mechanism results in a finite value at thermal equilibrium, $S_{iCE,0}$, given by inserting the electron thermal equilibrium polarization distribution into eq. 17. The normalized $S_{iCE}(\omega_{excite})$ spectrum can then contribute a maximum nuclear enhancement equal to $E^{max}_{iCE}(\omega_{excite}) = S_{iCE}(\omega_{excite})/S_{iCE,0}$. In practice, the iCE contribution to $E_n(\omega_{excite})$ can be smaller than this maximal value, due for example to the effect of the nuclear spin-lattice relaxation. To be able to choose the proper k_{iCE} value, while leaving the thermal equilibrium enhancement equal to 1, we subtract $S_{iCE,0}$ from $S_{iCE}(\omega_{excite})$ and add a one to $E_n(\omega_{excite})$ in Eq. 12. A consequence of these considerations is that $k_{iCE} \leq S^{-1}_{iCE,0}$, and therefore in the case of $|E_n(\omega_{excite})| > |E^{max}_{iCE}(\omega_{excite})|$ there must be other contributions to the enhancement apart from the iCE mechanism.

5 Simulations of the DNP line shapes

Using the above expressions we can now calculate the basic DNP spectra. This will be done for the 40mM TEMPOL sample described above at T =10, 20, and 40 K. However, before doing so we must first derive the $P_e(\omega_{detect}; \omega_{excite})$ profiles from the ELDOR experiments[48]. In the following we express all values of the frequencies ω_ς in units of Hertz and with respect to a central frequency, i.e. $\delta\nu_\varsigma = \omega_\varsigma/2\pi - 95$ GHz.

5.1 The electron polarization distribution - experiments and simulations

5.1.1 ELDOR measurements

ELDOR spectra as a function of the MW excitation frequency, $S^{exp}_e(\delta\nu_{excite})$, were recorded for several detection frequencies $\delta\nu_{detect}$ and temperatures T,using an irradiation time t_{excite} of the order of $5T_{1n}$. These long times were chosen in order for the sample to reach steady state values, thus avoiding possible time dependences of the ELDOR and DNP line-shapes at shorter times[38, 48]. The recorded EPR echo signals had to be shifted by subtracting a baseline signal that did not originate from the spin system itself. In order to take this baseline correction into account the measured signals detected at different $\delta\nu_{detect}$ frequencies were rescaled using

$$E^{exp}_{excite}(\delta\nu_{excite}) = \frac{S^{exp}_{e}(\delta\nu_{excite})/S^{exp}_{0} - S_b/S^{exp}_{0}}{1 - S_b/S^{exp}_{0}}, \tag{19}$$

where S^{exp}_{0} thermal equilibrium EPR signal, and S_b is a baseline signal at a given $\delta\nu_{detect}$ and T which probably originates from receiver ring down after the detection pulses. The value of S^{exp}_{0} was determined by measuring $S^{exp}_{e}(\delta\nu_{excite})$ for a set of far off resonance irradiation frequencies $\delta\nu_{excite}$ (in the range of -600 to -520 MHz) and taking their averaged value $\overline{S^{exp}_{e}}(\delta\nu_{excite}) = S^{exp}_{0}$. The S_b/S^{exp}_{0} value takes care of the fact that $E^{exp}_{excite}(\delta\nu_{excite,j}) \neq 0$ even under full saturation. An example of this procedure is given in the SI. In the case where S_b/S^{exp}_{0} is known, the $E^{exp}_{excite}(\delta\nu_{eexcite})$ functions becomes equal to the normalized polarization at $\delta\nu_{detect}$ for an irradiation at $\delta\nu_{excite}$:

$$E^{exp}_{excite}(\delta\nu_{excite}) = \frac{P^{exp}_{e}(\delta\nu_{detect}; \delta\nu_{excite})}{P^{exp}_{e0}(\delta\nu_{detect})}, \tag{20}$$

Thus, after the proper baseline correction the measured $E^{exp}_{excite}(\delta\nu_{excite})$ curves can be compared with simulated profiles of the normalized electron polarizations.

Unfortunately, in our experiments the values of S_b/S^{exp}_{0} could not be obtained experimentally, and therefore it was necessary to determine these values by adding them to the fitting parameters for creating simulated E^{sim}_{excite} curves that compare well with experimental ones.

In Fig. 6a-c (symbols) the corrected $E^{exp}_{excite}(\delta\nu_{excite})$ curves at T equal to 10 (black), 20 (blue), and 40 (red) K are plotted for three $\delta\nu_{detect}$ values given by (a) -140 MHz , (b) 0, and (c) 100 MHz. The S_b/S^{exp}_{0} values summarized in Table 2.

5.1.2 Electron polarization simulations

Next we must obtain the values of $P_e(\delta\nu_{detect}, \delta\nu_{excite})$, needed for the derivation of the DNP line shapes, by fitting simulated ELDOR spectra to the measured ones. The simulations were conducted as explained in section 2.2.2. $P_{e,j}(\delta\nu_{excite,j'})$ values were simulated as a function of $\delta\nu_{excite,j'}$, with $\delta\nu_j = \delta\nu_{detect}$. Normalizing with respect to the their thermal value, $P^0_{e,j}$, results in normalized ELDOR spectra

$$E^{sim}_{excite}(\delta\nu_{excite,j'}) = \frac{P_{e,j}(\delta\nu_{excite,j'})}{P^0_{e,j}}, \tag{21}$$

in analogy with eq. 20. In order to reduce over-saturation around $\delta\nu_j = \delta\nu_{excite,j'}$, as explained in Ref. [48], the output of the simulations was smoothed using

$$E_{excite}^{sim'}(\delta\nu_{excite,j'}) = \frac{1}{2}E_{excite}^{sim}(\delta\nu_{excite,j'})+\frac{1}{4}E_{excite}^{sim}(\delta\nu_{excite,(j'-1)})+\frac{1}{4}E_{excite}^{sim}(\delta\nu_{excite,(j'+1)}). \quad (22)$$

These distributions were then fitted to the experimental ELDOR spectra $E_{excite}^{exp}(\delta\nu_{excite})$ using a single set of parameters (Table 3), apart for the S_b/S_0^{exp} parameter (Table 2), that was chosen for each data set, and the T_{1e} and T_{1n} values which were taken from measurements (Table 4). The resulting $E_{excite}^{sim'}(\delta\nu_{excite,j'})$ profiles are plotted in Fig. 6a-c (solid lines), showing good agreement with the experimental spectra for the different temperatures and $\delta\nu_{detect}$ values. A single Λ^{eSD} parameter was found that resulted in a good fit between the simulated E_{excite}^{sim} profiles and the ELDOR spectra at all temperatures. In general the eSD rates can be expected to be temperature dependent, when we realize that the spin fluctuations responsible for the eSD process can be T_{1e} dependent or can become quenched at very low temperatures[55, 44, 56]. The value of $\overline{A}^{\pm}$ could not be determined accurately from the ELDOR measurements because no clear features originating from the SE were observed. Thus this value was chosen during the DNP simulations where SE features are present, as will be explained in section 5.3. It is important to note that while echo detection close to the center of the EPR line results in the highest signals, the ELDOR spectra acquired at the sides of the EPR line exhibit more spectral features than the ones measured at the center. Namely, the spectra acquired at $\delta\nu_{detect} = -140$, and to a lesser degree the one acquired at 100 MHz, were more helpful for finding the proper fitting parameters, although they required longer signal averaging to obtain the same SNR as the spectra detected at $\delta\nu_{detect} = 0$.

Using the set of parameters that creates a good fit between $E_{excite}^{sim'}(\omega_{excite,j'})$ and $E_{excite}^{exp}(\omega_{excite})$ it is possible to calculate the $P_e(\delta\nu_{detect}, \delta\nu_{excite})$ profiles needed for the DNP line-shape simulations (section 4). As an example of the profiles derived from these equations, the normalized electron polarization profiles $P_e(\delta\nu_{detect}, \delta\nu_{excite})/P_{e0}(\delta\nu_{detect})$ are plotted in Fig. 6d-f for $\delta\nu_{excite}$ = -140 (d) , 0 (e), and 100 (f) MHz. As can be seen, irradiation close to the center of the EPR line results in larger depolarization across the whole EPR spectrum, while irradiation closer to the edge the depolarization is much more localized around $\delta\nu_{excite}$. This is a result of the dependence of the eSD rate on the EPR line-shape, as explained in Ref. [48]. In addition, higher depolarizations can be seen at lower temperatures, mainly because T_{1e} increases at low temperatures while the eSD rate remains the same, as given by the constant Λ^{eSD} coefficient.

Figure 6: (a-c) Measured (square symbols) and simulated (lines) steady state E_{excite} profiles,detected at $\delta\nu_{detect}$ equal to -140 MHz (a), 0 MHz (b), and 100 MHz (c), as indicated by the gray arrows, and at temperatures equal to 40 K (red), 20 K (blue), and 10 K (black). The experimental signals were corrected as in eq. 19 with S_b/S_0^{exp} values given in Table 2. The simulations were performed using the parameters given in Table 3 and the relaxation parameters given in Table 4, and their results smoothed as in eq. 22. (d)-(e) Simulated steady state electron polarization distributions $P_e(\delta\nu_{detect})/P_{e,0}(\delta\nu_{detect})$ derived from ELDOR/DNP data obtained for MW irradiation frequencies $\delta\nu_{excite}$ equal to -140 MHz (a), 0 MHz (b), and 100 MHz (c), as indicated by the gray arrows. The same color-codings indicate the temperatures as for the E_{excite} profiles. The EPR line shape of TEMPOL[36] is given by the gray line at the top.

$\delta\nu_{detect}$ (MHz)	-140	0	100
10 K	0	0	0.25
20 K	-0.1	-0.1	.1
40 K	-0.4	0	0

Table 2: Fitted S_b/S_0^{exp} values used to remove the baseline artifact from the experimental ELDOR spectra. These were used to generate E_{excite}^{exp} spectra, using eq. 19, with the results plotted as square symbols in Fig. 6.

Parameter	Value
$\Delta_{bin}/2\pi$	2 MHz
$\omega_1/2\pi$	0.6 MHz
T_{2e}	10 μs
Λ^{eSD}	1000 $(\mu\text{s})^{-3}$
$\overline{A}^{\pm}/2\pi$	0.7 MHz

Table 3: Simulation parameters used for the calculation of the electron polarization profiles, P_e. Relaxation parameters at the different temperatures were taken from Table 4. The EPR line shape was taken from Ref. [36] and a proton frequency of $\omega_n/2\pi$=144 MHz was used.

	T_{1n}(s)	T_{1e}(ms)
40 K	5	0.8
20 K	7.1	5.3
10 K	8.5	17

Table 4: Electron and nuclear spin-lattice relaxation times. These were obtained by fitting saturation recovery curves, measured as explained in sec. 2.1.

	T_{1n}(s)	T_{BU}(s)
40 K	5.0	5.0
20 K	7.1 (7.1)	7.0 (6.6)
10 K	8.4	8.3

Table 5: Electron and nuclear spin-lattice relaxation times. These were obtained by fitting saturation recovery curves, measured as explained in sec. 2.1.

5.2 The individual DNP line shapes

After deriving the $P_e(\delta\nu_{detect}, \delta\nu_{excite})$ profiles from the ELDOR data, we can now calculate the basic $S_{SE}(\delta\nu_{excite})$, $S_{dCE}(\delta\nu_{excite})$, and $S_{iCE}(\delta\nu_{excite})$ DNP line-shapes using eqs. 13-17. In practice the integrations in these expressions were removed and the $S_M(\delta\nu_{excite})$ line-shapes were calculated using a discrete set of excitation and detection frequencies $\{\delta\nu_j\}$ with a resolution of $|\delta\nu_j - \delta\nu_{j-1}|$ =2MHz, equal to the bin size used in the ELDOR simulations (section 5.1.2). Thus the relevant values of the $P_e(\delta\nu_{detect}, \delta\nu_{excite})$ profiles are defined by $P_{e,j}(\delta\nu_{j_{excite}})$, with $\delta\nu_{detect} = \delta\nu_j$ and $\delta\nu_{excite} = \delta\nu_{j_{excite}}$. These discrete frequency values require a definition for the weight-functions $g_{SE}(\delta\nu)$, $g_{dCE}(\delta\nu, \delta\Omega)$, and $g_{iCE}(\delta\Omega)$ with bin-width resolution. In our calculations we set these functions equal to one for $\delta\nu, \delta\Omega$=0 and zero otherwise, thus considering only on resonance irradiation on the DNP transitions and a CE condition width which is within the bin size. As a result, the expressions for the DNP shapes can be simplified to:

$$S_{SE}(\delta\nu_{j_{excite}}) = N_{SE}^{-1}\{f_{j^-_{excite}} P_{e,j^-_{excite}}(\delta\nu_{j_{excite}}) - f_{j^+_{excite}} P_{e,j^+_{Mexcite}}(\delta\nu_{j_{excite}})\}, \tag{23}$$

for the SE DNP;

$$S_{dCE}(\delta\nu_{j_{excite}}) = N_{dCE}^{-1}\, f_{j_{excite}}\{f_{j^-_{excite}} s_{CE,j_{excite}}(\delta\nu_{j_{excite}}) - f_{j^+_{excite}} s_{CE,j^+_{excite}}(\delta\nu_{j_{excite}})\}, \tag{24}$$

for the dCE DNP; and

$$S_{iCE}(\delta\nu_{j_{excite}}) = N_{dCE}^{-1} \sum_j f_j\, f_{j^-} s_{CE,j}(\delta\nu_{j_{excite}}), \tag{25}$$

for the iCE DNP, with

$$s_{CE,j}(\delta\nu_{j_{excite}}) = \frac{P_{e,j}(\delta\nu_{j_{excite}}) - P_{e,j^-}(\delta\nu_{j_{excite}})}{1 - P_{e,j}(\delta\nu_{j_{excite}}) \times P_{e,j^-}(\delta\nu_{j_{excite}})}. \tag{26}$$

Here $P_{j_{excite}}$ and $f_{j_{excite}}$ correspond to the polarization and electron fraction in the $\delta\nu_{j_{excite}} = \delta\nu_{excite}$ frequency bin, and $P_{j^\pm}$ and $f_{j^\pm}$ to the $\delta\nu_{j^\pm} = \delta\nu_j \pm \nu_n$ frequency bin. As discussed above, the equilibrium $S_{iCE,0}$ value can be calculated by inserting the thermal electron polarization distribution into eq. 25, and can be used to determine the maximum iCE enhancement contribution $E^{max}_{iCE}(\delta\nu_i)$.

Using the above expressions the basic DNP spectra were calculated relying on the $P_{e,j}(\delta\nu_{j_{excite}})$ profiles obtained from the parameters in Tables 3 and 4, as in Fig. 6. The results of these calculations are shown in Fig. 7 for 10 K (black), 20 K (blue), and 40 K (red). As can be seen there is a clear change in the DNP spectra as a function of temperature: the separation between the enhancement maxima and minima becomes larger at lower temperatures, and the relative enhancement far from the center of the EPR line increases. This is because the eSD is more prominent when irradiating at the center of the EPR line than at the sides, and because its effect increases with decreasing temperature, as was shown in Fig. 6d-e. It can also be seen that $S_{iCE}(\delta\nu_{j_{excite}})$ shows enhancements outside of the EPR line, due to the loss of electron polarization *via* the SE mechanism, which depends on the value for $\overline{A}^{\pm}$. The maximum and minimum value of the $E^{max}_{iCE}(\delta\nu_j)$ profile are tabulated in table 6. The change in the actual enhancement of the different mechanisms with temperature, and in particular its dependence on the eSD mechanism, is left for future studies.

Figure 7: SE (a), dCE (b), and iCE (c) DNPprofiles calculated using eqs. 23-25. The simulated electron polarization profiles were obtained by fitting the 40 K (red) 20 K (blue) and 10 K (black) E_{excite} ELDOR data (see Fig. 6) by using the parameters of Tabs. 3 and 4. All profiles were normalized with respect to the average of the magnitudes of the enhancement at its maximum and minimum. The EPR line-shape of TEMPOL[36] is given by the gray line at the top of the figure.

	E^{exp}_n		E^{max}_{iCE}	
	Maximum	Minimum	Maximum	Minimum
40 K	46	-54	74	-114
20 K	50	-62	87	-120
10 K	42	-44	62	-70

Table 6: The maximum and minimum DNP enhancements at different temperatures. The experimental values E^{exp}_n were evaluated by comparing the maximal detected signal with a reference thermal equilibrium signal, and the maximal predicted iCE enhancements by calculating the $E^{max}_{iCE} = S_{iCE}(\delta\nu_{j_{excite}})/S_{iCE,0}$ values, as described in section 4.

5.3 The DNP simulations

Finally, we can combine the simulated DNP line-shapes as in eq. 12 in order to reconstruct the experimental DNP enhancement spectra $E^{exp}_n(\delta\nu_{excite})$. These spectra after normalization by the average of the magnitudes of the enhancement at its maximum and minimum, are plotted in Fig. 8. The maximum and minimum values of $E_n^{exp}(\delta\nu_{excite})$ are given in Table 6. In practice, after adjusting the $\overline{A}^{\pm}$ value (Table 3) as described in section 5.1.2, , we found a good agreement between the experimental line-shapes and the iCE-DNP line-shape. These simulated spectra are plotted again in Fig. 8 (red lines), as well as the difference between the two normalized curves (gray dashed lines). A clear difference between the two can be seen around the center of the EPR line, however the width, relative intensities and the features at the edges of the spectra are all reproduced. This indicates that in our TEMPOL sample the iCE mechanism is the leading mechanism. Since the detected enhancements are lower than their maximal iCE values (Table 6), no additional DNP is required to achieve the experimental enhancements. The simulated DNP enhancement outside of the EPR line shows that the SE mechanism plays a role at least in the form of a depolarization of the electrons, with possibly a small contribution to the DNP enhancement. No combination of the $S_{SE}(\delta\nu_{excite})$ and $S_{dCE}(\delta\nu_{excite})$ line-shapes was found that fitted the experimental DNP spectra satisfactory. This differed from the analysis presented in Ref. [36] on a similar sample, since here the effect of the eSD on these DNP mechanisms was introduced. However, more measurements are needed on a variety of samples to determine the actual role of the dCE mechanism during DNP. The source of the relatively large difference between the experiment and simulations at the center of the EPR line is not clear at the moment, and could not be accounted for by introducing the $S_{SE}(\delta\nu_{excite})$ and $S_{dCE}(\delta\nu_{excite})$ spectra. It may be a consequence of the assumptions made during the calculations of the $P_{e,j}(\delta\nu_{j_e})$ profiles or the basic $S_n(\delta\nu_{j_e})$ line-shapes, or from an additional DNP processes, such as the Overhauser Effect in solid dielectrics[57].

Figure 8: Measured (square symbols) and simulated iCE (red lines) DNP profiles. The measured spectra were obtained at 40 K (a), 20 K (b), and 10 K (c), using a t_{excite} values of about $5T_{1n}$. The simulated spectra were derived from eq. 25 using the parameters given in Tabs. 3 and 4. Both experimental and simulated data were normalized with respect to the average of the magnitudes of the enhancement at its maximum and minimum. The dashed gray line shows the difference between the measured and simulated normalized profiles. The EPR-line shape of TEMPOL[36] is given by the gray line at the top of the figure.

6 Summary and conclusions

In this paper we characterized the influence of the electron spectral diffusion (eSD) mechanism on the DNP spectra. First, the effect of the eSD on the nuclear polarization in electron-nuclear model systems was considered. There it was shown that in the case of the

CE, a change in the difference between the electron polarizations results also in a change of the nuclear polarization, due to the CE state mixing. This nuclear polarization is correlated to this difference, which can be the result of a direct MW irradiation on the CE electron pair (dCE) or from irradiation on other electrons that indirectly depolarize the CE electron pair *via* a eSD type of process (iCE). In particular, the relationship between the electron and nuclear polarizations were derived and checked numerically. Finally, the dependence of the nuclear enhancement on the CE condition, and the polarization buildup times were calculated for a model iCE system.

Following these calculations, the steady state SE , dCE, and iCE DNP line-shapes of real samples were simulated, in analogy to the work presented in Refs. [36, 37, 38] but this time taking the effects of the electron depolarization into account. This was possible after deriving the electron polarization distributions, using parameters that allowed simulated ELDOR spectra to be fitted with experimental ones[48]. In the present study ELDOR and DNP data were obtained from a 40 mM TEMPOL sample at 10, 20, and 40 K and the shapes of the three steady state basic DNP spectra were calculated for each temperature. It was shown that the electron polarization profiles strongly influence these shapes, including changes in the frequency separation between the maximum and minimum enhancements. In addition, it was shown that the maximal iCE contribution to the enhancement can also be calculated.

A comparison of the simulated basic DNP spectra with the experimental DNP spectra showed that the iCE mechanism can explain most of the detected spectral features at all three temperatures, and account for the measured enhancement values. This result differs from the DNP spectral analysis presented in Refs. [36, 37, 38], where the eSD and iCE mechanisms were not considered, and the changes in the DNP line-shapes as a function of temperature were interpreted as a change in the relative contribution of the dCE and SE mechanisms. In the present analysis the features originating from the SE are indirectly influencing the DNP results *via* the eSD induced depolarization of the electrons, and leading to iCE enhancements.

Future work must include an extension of the electron depolarization model[48] such that it will include also the iCE mechanism. This will allow for simultaneously fitting of both ELDOR and DNP experimental data both as function of frequency and of time, and also including the DNP enhancement values themselves. As such, new insight into the contributions of the MW irradiation and the different relaxation mechanisms, including the eSD, to the DNP enhancement will be gained. Further experiments are needed to reduce the number of fitted parameters used in our present model, and in order to determine the interplay between the different DNP mechanisms under various conditions, such as the MW power, radical type and sample characteristics.

Acknowledgments

We thank Dr. Alberto Rosso for fruitful discussions regarding the CE mechanism. This work was supported by the German-Israeli Project Cooperation of the DFG through a special allotment by the Ministry of Education and Research (BMBF) of the Federal republic of Germany. This research was also made possible in part by the historic generosity of the Harold Perlman Family. D.G holds the Erich Klieger Professorial Chair in Chemical Physics.

References

[1] A. Overhauser, *Phys. Rev.*, 1953, **92**(2), 411–415.

[2] T. R. Carver and C. P. Slichter, *Phys. Rev.*, 1953, **92**(1), 212–213.

[3] C. Jeffries, *Phys. Rev.*, 1957, **106**(1), 164–165.

[4] R. A. Wind, M. J. Duijvestijn, C. van der Lugt, A. Manenschijn, and J. Vriend, *Prog. Nuc. Mag. Res. Sp.*, 1985, **17**, 33–67.

[5] M. Afeworki, S. Vega, and J. Schaefer, *Macromolecules*, 1992, **25**(16), 4100–4105.

[6] M. Afeworki, R. A. McKay, and J. Schaefer, *Macromolecules*, 1992, **25**(16), 4084–4091.

[7] M. Afeworki and J. Schaefer, *Macromolecules*, 1992, **25**(16), 4092–4096.

[8] L. R. Becerra, G. J. Gerfen, R. J. Temkin, D. J. Singel, and R. G. Griffin, *Phys. Rev. Lett.*, 1993, **71**(21), 3561–3564.

[9] G. J. Gerfen, L. R. Becerra, D. A. Hall, R. G. Griffin, R. J. Temkin, and D. J. Singel, *J. Chem. Phys.*, 1995, **102**(24), 9494.

[10] D. A. Hall, D. Maus, G. J. Gerfen, S. J. Inati, L. R. Becerra, F. W. Dahlquist, and R. G. Griffin, *Science*, 1997, **276**(5314), 930–932.

[11] J. H. Ardenkjaer-Larsen, B. Fridlund, A. Gram, G. Hansson, L. Hansson, M. H. Lerche, R. Servin, M. Thaning, and K. Golman, *Proc. Natl. Acad. Sci. U.S.A.*, 2003, **100**(18), 10158–63.

[12] A. V. Kessenikh, V. I. Luschikov, A. A. Manenkov, and Y. V. Taran, *Sov. Phys. Solid State*, 1963, **5**, 321–329.

[13] A. V. Kessenikh, V. I. Luschikov, and A. A. Manenkov, *Sov. Phys. Solid State*, 1963, **5**, 835–837.

[14] A. V. Kessenikh, A. A. Manenkov, and G. I. Pyatnitskii, *Sov. Phys. Solid State*, 1964, **6**, 641–643.

[15] C. Hwang and D. Hill, *Phys. Rev. Lett.*, 1967, **18**(4), 110–112.

[16] C. Hwang and D. Hill, *Phys. Rev. Lett.*, 1967, **19**(18), 1011–1014.

[17] D. Wollan, *Phys. Rev. B*, 1976, **13**(9), 3671–3685.

[18] V. A. Atsarkin, G. A. Vasneva, and E. Novikov, *Sov. Phys. JETP*, 1975, **41**(4), 746–751.

[19] J. van Houten, W. T. Wenckebach, and N. Poulis, *Physica B+C*, 1977, **92**(2), 210–220.

[20] S. Stoll, B. Epel, S. Vega, and D. Goldfarb, *J. Chem. Phys.*, 2007, **127**(16), 164511.

[21] K.-N. Hu, G. T. Debelouchina, A. A. Smith, and R. G. Griffin, *J. Chem. Phys.*, 2011, **134**(12), 125105.

[22] Y. Hovav, A. Feintuch, and S. Vega, *J. Magn. Reson.*, 2012, **214**(1), 29–41.

[23] K. R. Thurber and R. Tycko, *J. Chem. Phys.*, 2012, **137**(8), 084508.

[24] F. Mentink-Vigier, U. Akbey, Y. Hovav, S. Vega, H. Oschkinat, and A. Feintuch, *J. Magn. Reson.*, 2012, **224**, 13–21.

[25] M. Borghini and K. Scheffler, *Phys. Rev. Lett.*, 1971, **26**(22), 1362–1365.

[26] S. F. J. Cox, V. Bouffard, and M. Goldman, *J. Phys. C Solid State Phys.*, 1973, **6**(5), L100–L103.

[27] W. de Boer, M. Borghini, K. Morimoto, T. O. Niinikoski, and F. Udo, *J. Low Temp. Phys.*, 1974, **15**(3-4), 249–267.

[28] W. de Boer, *J. Low Temp. Phys.*, 1976, **22**(1-2), 185–212.

[29] A. Abragam and M. Goldman, *Reports Prog. Phys.*, 1978, **41**(3), 395–467.

[30] F. Kurdzesau, B. van den Brandt, A. Comment, P. Hautle, S. Jannin, J. J. van der Klink, and J. A. Konter, *J. Phys. D-Appl. Phys.*, 2008, **41**(15), 155506.

[31] J. H. Ardenkjaer-Larsen, S. Macholl, and H. Johannesson, *Appl. Magn. Reson.*, 2008, **34**(3-4), 509–522.

[32] S. Jannin, A. Comment, F. Kurdzesau, J. . Konter, P. Hautle, B. van den Brandt, and J. J. van der Klink, *J. Chem. Phys.*, 2008, **128**(24), 241102.

[33] L. L. Lumata, A. K. Jindal, M. E. Merritt, C. R. Malloy, A. D. Sherry, and Z. Kovacs, *J. Am. Chem. Soc.*, 2011, **133**(22), 8673–80.

[34] L. L. Lumata, M. E. Merritt, C. R. Malloy, A. D. Sherry, and Z. Kovacs, *Appl. Magn. Reson.*, 2012, **43**(1-2), 69–79.

[35] S. Jannin, A. Comment, and J. J. Klink, *Appl. Magn. Reson.*, 2012, **43**(1-2), 59–68.

[36] D. Shimon, Y. Hovav, A. Feintuch, D. Goldfarb, and S. Vega, *Phys. Chem. Chem. Phys.*, 2012, **14**(16), 5729–43.

[37] D. Banerjee, D. Shimon, A. Feintuch, S. Vega, and D. Goldfarb, *J. Magn. Reson.*, 2013, **230**, 212–9.

[38] D. Shimon, A. Feintuch, D. Goldfarb, and S. Vega, *Phys. Chem. Chem. Phys.*, 2014, **16**(14), 6687–99.

[39] Y. Hovav, A. Feintuch, and S. Vega, *J. Magn. Reson.*, 2010, **207**(2), 176–189.

[40] J. Klauder and P. Anderson, *Phys. Rev.*, 1962, **125**(3), 912–932.

[41] W. B. Mims, *Electron Spin Echoes*, Plenum, New York, 1972.

[42] A. M. Raitsimring, K. M. Salikhov, S. F. Bychkov, and Y. D. Tsvetkov, *Sov. Phys. Solid State*, 1975, **17**(2), 303–306.

[43] K. M. Salikhov and Y. D. Tsvetkov, *Electron Spin-Echo Studies of Spin-Spin Interactions in Solids*, Wiley, New York, 1979.

[44] S. A. Dzuba and A. Kawamori, *Concepts Magn. Reson.*, 1996, **8**(1), 49–61.

[45] T. Siaw, M. Fehr, A. Lund, A. Latimer, S. A. Walker, D. T. Edwards, and S.-I. Han, *Phys. chem. chem. phys.*, 2014, **16**(35), 18694–706.

[46] P. Schosseler, T. Wacker, and A. Schweiger, *Chem. Phys. Lett.*, 1994, **224**(3-4), 319–324.

[47] J. Granwehr and W. Kockenberger, *Appl. Magn. Reson.*, 2008, **34**(3-4), 355–378.

[48] Y. Hovav, I. Kaminker, D. Shimon, A. Feintuch, D. Goldfarb, and S. Vega, *Phys. Chem. Chem. Phys.*, 2014, (doi: 10.1039/C4CP03825H).

[49] A. Feintuch, D. Shimon, Y. Hovav, D. Banerjee, I. Kaminker, Y. Lipkin, K. Zibzener, B. Epel, S. Vega, and D. Goldfarb, *J. Magn. Reson.*, 2011, **209**(2), 136–41.

[50] B. Epel, I. Gromov, S. Stoll, A. Schweiger, and D. Goldfarb, *Concepts Magn. Reson. Part B Magn. Reson. Eng.*, 2005, **26B**(1), 36–45.

[51] Y. Hovav, A. Feintuch, and S. Vega, *J. Chem. Phys.*, 2011, **134**(7), 074509.

[52] Y. Hovav, A. Feintuch, and S. Vega, *Phys. Chem. Chem. Phys.*, 2013, **15**(1), 188–203.

[53] S. Colombo Serra, M. Filibian, P. Carretta, A. Rosso, and F. Tedoldi, *Phys. Chem. Chem. Phys.*, 2013.

[54] Y. Hovav, O. Levinkron, A. Feintuch, and S. Vega, *Appl. Magn. Reson.*, 2012, **43**(1-2), 21–41.

[55] A. Abragam, *The Principles of Nuclear Magnetism*, Oxford University Press, London, 1961.

[56] S. Takahashi, R. Hanson, J. Van Tol, M. S. Sherwin, and D. D. Awschalom, *Phys. Rev. Lett.*, 2008, **101**(July), 1–4.

[57] T. V. Can, M. a. Caporini, F. Mentink-Vigier, B. Corzilius, J. J. Walish, M. Rosay, W. E. Maas, M. Baldus, S. Vega, T. M. Swager, and R. G. Griffin, *J. Chem. Phys.*, 2014, **141**(6), 064202.

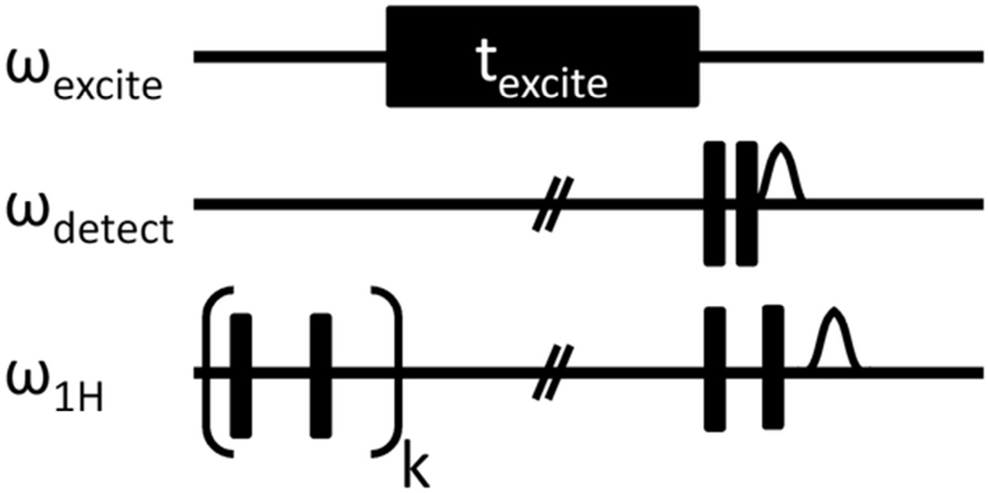

26x13mm (600 x 600 DPI)

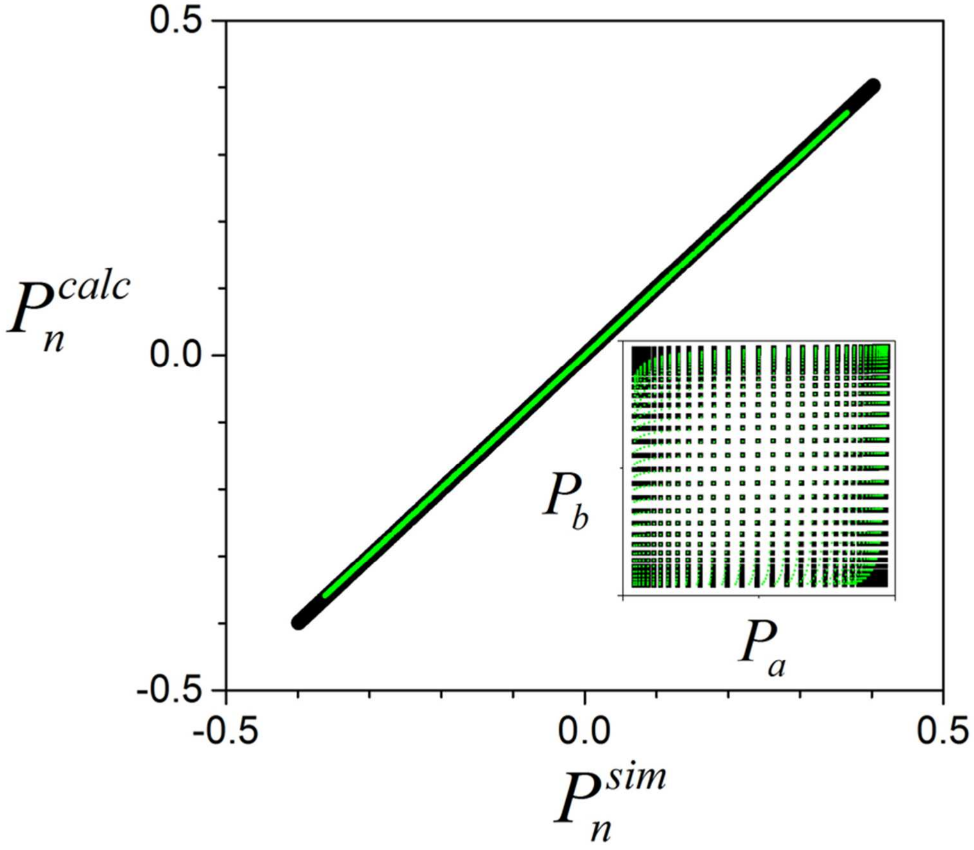

74x65mm (300 x 300 DPI)

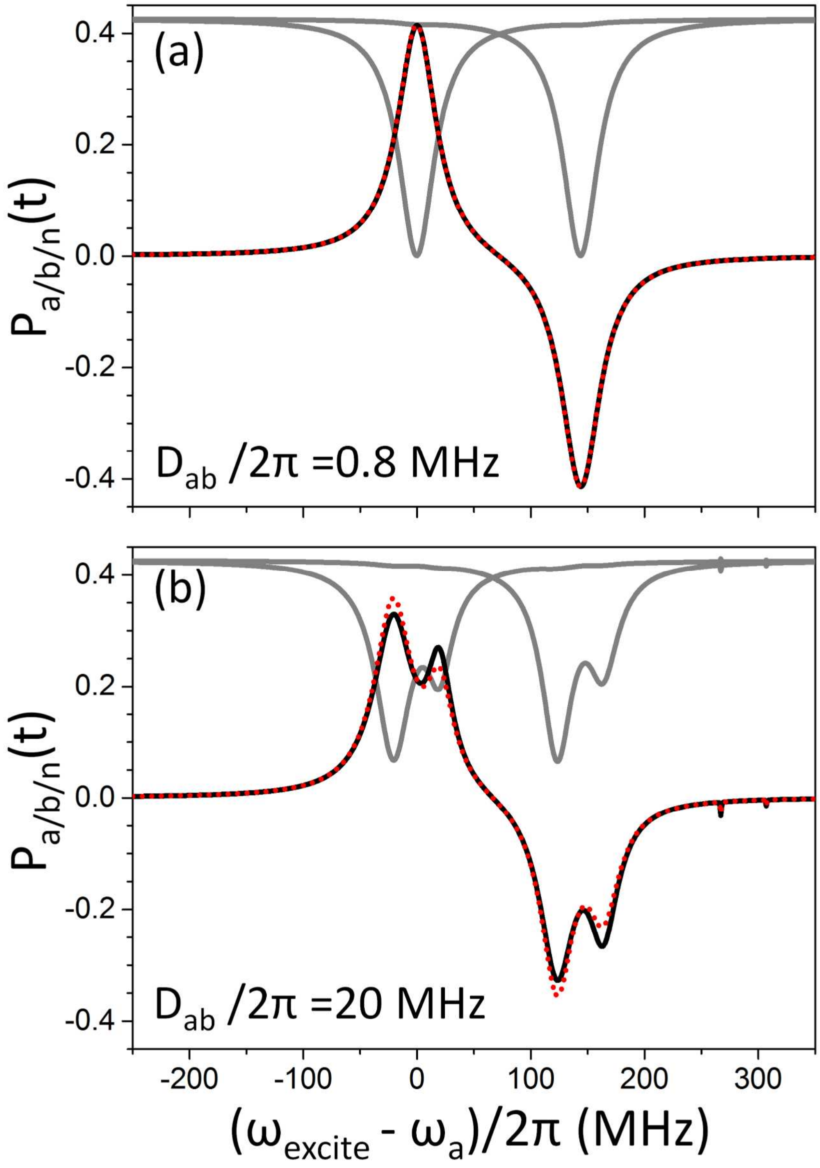

114x155mm (600 x 600 DPI)

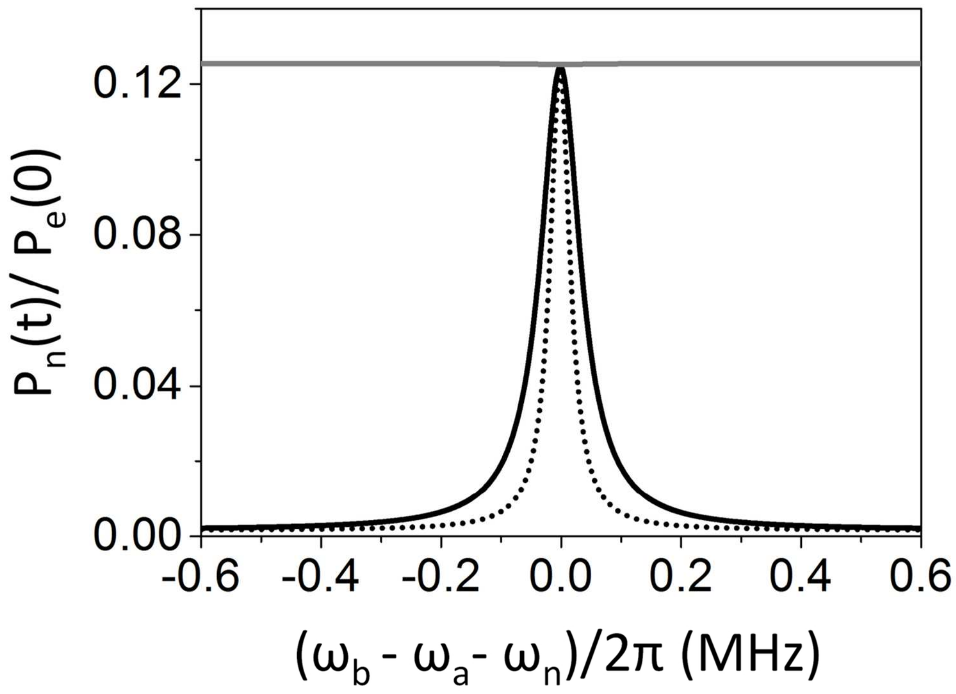

61x44mm (600 x 600 DPI)

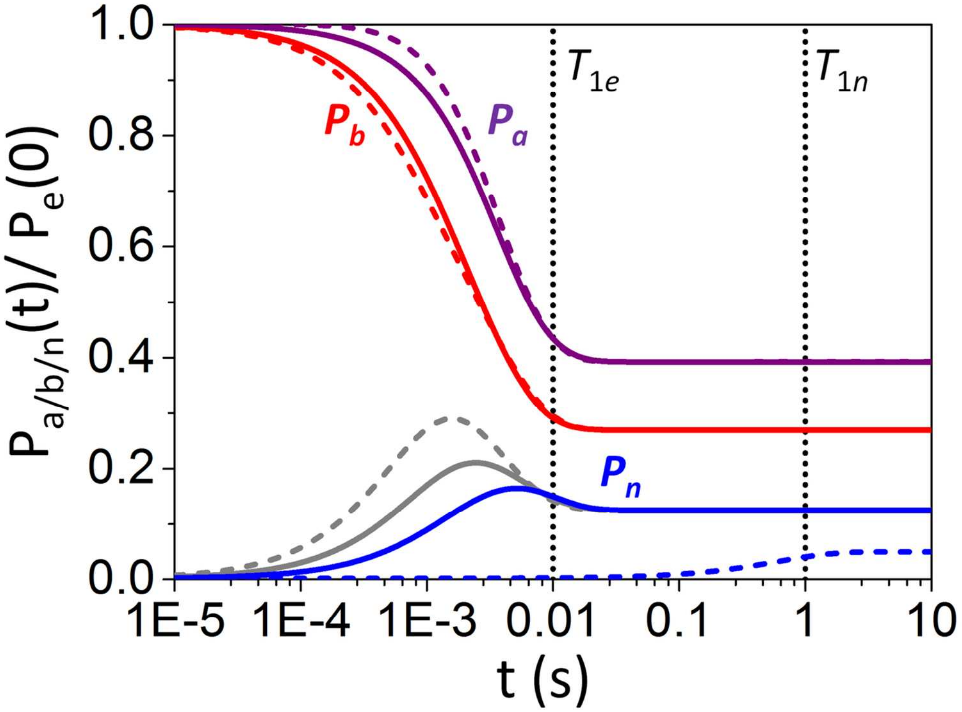

62x45mm (600 x 600 DPI)

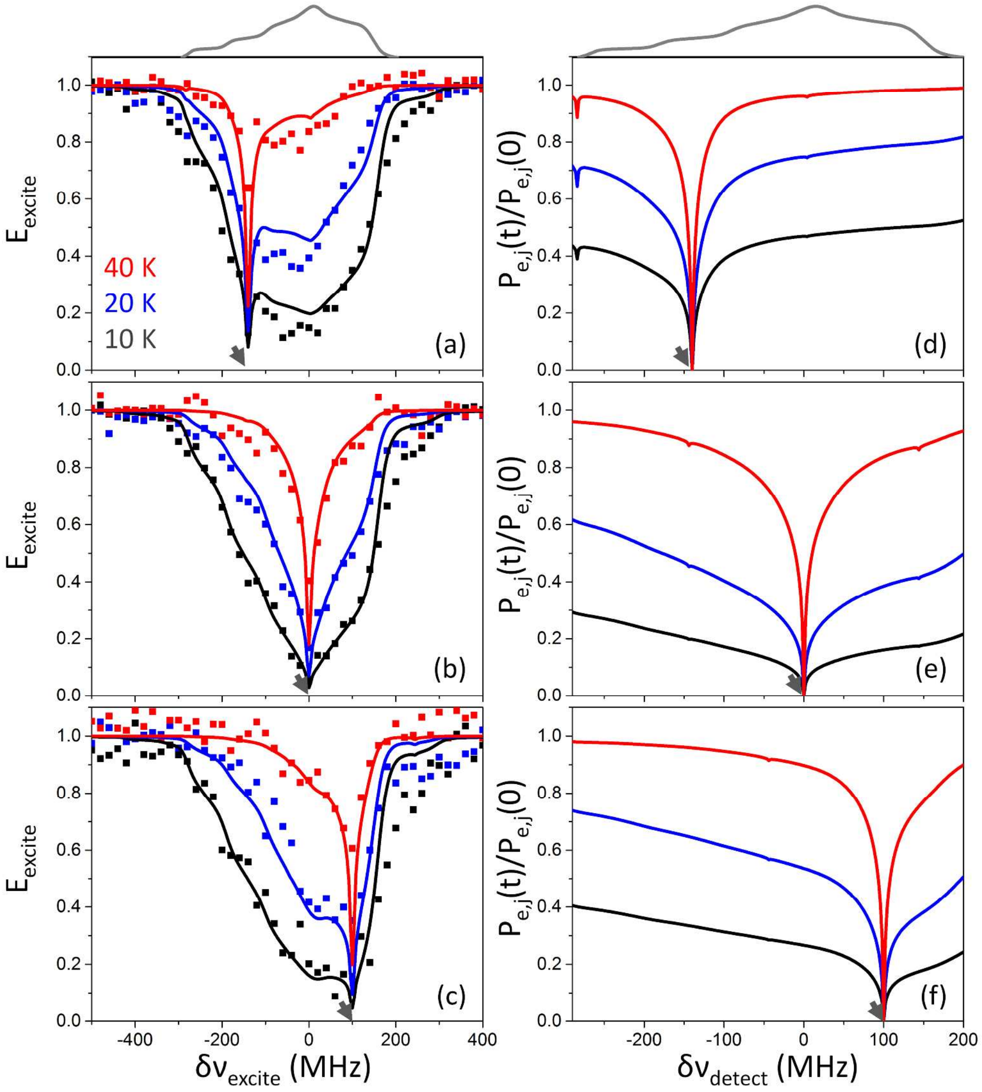

166x184mm (600 x 600 DPI)

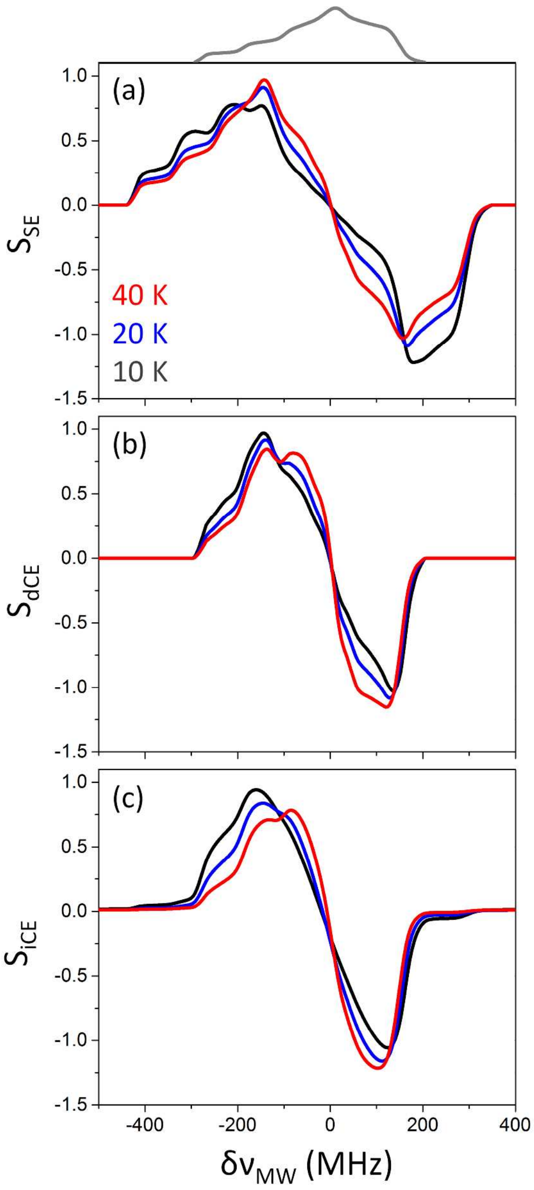

183x396mm (600 x 600 DPI)

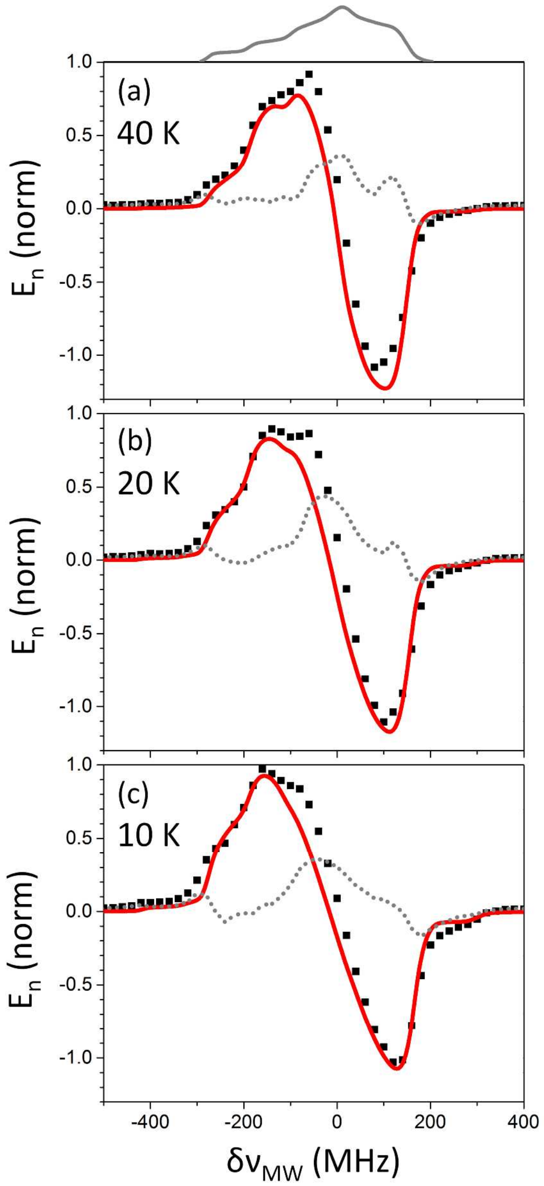

180x381mm (600 x 600 DPI)